An experimental investigation of the development and permeability of clay smears along faults in uncemented sediments

F. Cuisiat*, E. Skurtveit

Norwegian Geotechnical Institute, P.O. Box 3930, Ullevaal Stadion, N-0806 Oslo, Norway

A B S T R A C T

The generation of clay smears along faults in uncemented sediments has been studied through laboratory experiments in a newly developed high stress ring shear apparatus. The main objective is to investigate basic mechanisms involved in the deformation process of sediments during faulting and formation of clay smears.

The experimental test program comprises ring shear tests on sand with embedded clay segments (sand–clay sequence) under constant effective normal stress. Visual inspection of the samples after testing, analyses of thin sections and permeability measurements across the shear zone are used to characterise geometrical continuity, thickness and sealing potential of the smear. Deformation processes such as grain reorientation, clay smear and cataclasis are identified from the tests. The complexity of the shear zone is observed to increase with the effective normal stress applied to the specimen and the number of clay segments used in the ring (multilayered sand–clay sequences). At low effective normal stress, in clay-rich sediments, clay smear is the most efficient mechanism for permeability reduction. The permeability across the smear decreases with ring rotation (or shear displacement) and effective normal stress. A maximum decrease of two orders of magnitude compared to the permeability of the surrounding sand is observed after 90° rotation under 10.5 MPa effective normal stress. Sand–sand juxtaposition shear is dominated by grain rolling causing only minor permeability reduction. At high effective normal stress, permeability measurements across clay smear and sand–sand juxtaposition yield similar values indicating that the permeability reduction is dominated by grain size reduction in the sand.

© 2009 Elsevier Ltd. All rights reserved.

1. Introduction

Faults play a major role in the distribution and movement of fluids, hydrocarbons or groundwater in the Earth's crust. Faults may act as barriers, baffles, or mixed conduit-barrier systems to fluid flow depending on the composition of the faulted rock, the stress conditions at the time of faulting, and post-faulting burial and temperature history (Antonellini et al., 1994; Caine et al., 1996; Sibson, 2000). An understanding of fault zone internal structure and associated hydraulic properties is a requisite to many fields such as petroleum exploration and production, groundwater modelling, earthquake rupture, and sequestration of CO_2 (e.g. Hickman et al., 1995; Sibson, 2000; Bense and Van Balen, 2004; Rutqvist et al., 2007; Annunziatellis et al., 2008; Wibberley et al., 2008).

Faults in sediments can be classified upon the phyllosilicate content of their host lithology and burial depth at time of faulting (Fisher and Knipe, 1998, 2001). Faults in clean sandstones (<15% clay) at shallow depth produce a disaggregation zone with only local grain rearrangement, no grain-fracturing and similar or even higher permeability than the host rock (Fisher and Knipe, 2001; Bense and Van Balen, 2004). Faulting of the same sediments at greater depth results in grain-fracturing (cataclasis) with clogging of the pore space by smaller grain fragments. Experimental data show that the onset of grain-fracturing may start at depths as low as 500 m, or 5 MPa effective vertical stress (Chuhan et al., 2002). Post-faulting burial may lead to quartz cementation for temperatures greater than circa 90 °C or circa 3 km in basins with normal temperature gradient. Quartz cementation occurs most intensively at burial depths between 3.5 and 5 km (120–170 °C) (Björlykke and Höeg, 1997). In impure sands with clay content between 15 and 40%, or other contexts of similar mineralogy, faulting leads to a fault gouge or phyllosilicate framework fault rock (Fisher and Knipe, 2001) with mixing of sand and clay often structured parallel to the

shear plane (Rutter et al., 1986; Wibberley and Shimamoto, 2003; van der Zee and Urai, 2005).

In clay-rich sequences (i.e. clay content higher than 40%), faulting is commonly associated with clay smears, that is shearing of an offset clay layer into the fault zone (Fig. 1).

Smearing of low permeability clay has been presented as one of the most efficient mechanism for fault sealing. From outcrop observations, laboratory experiments, and numerical modelling (e.g. Lindsay et al., 1993; Lehner and Pilaar, 1997; van der Zee and Urai, 2005; Sperrevik et al., 2000; Clausen and Gabrielsen, 2002; Egholm et al., 2008) several processes have been suggested to explain the occurrence of clay smear such as: clay abrasion, lateral clay injection from source layer and shearing within fault, and material instabilities. Nevertheless, no real mechanics-based predictive model for fault seals is yet available in the literature.

In this paper, we present the results of ring shear experiments to study the development and permeability of clay smear along faults. The use of a ring shear apparatus in geosciences is fairly widespread, for instance to characterise the residual shear strength and behaviour of soils and granular materials as well as the interaction between soil and structure (e.g. Bishop et al., 1971; Tika et al., 1996; Lupini et al., 1981; Hungr and Morgenstern, 1984; Sassa et al., 2003). However, the use of a ring shear device as an analogue for fault formation and clay smear is more limited, although some early work was conducted by Mandl et al. (1977). The principle is illustrated in Fig. 2. The ring shear sample consists of an annular sand specimen confined between upper and lower rings. One or several segments of clay are embedded within the sand. After applying the vertical (normal) stress σ_n onto the specimen, the lower ring is rotated, thus dragging the clay material onto the shear plane located at the separation of the upper and lower confining rings. The linear displacement along the shear plane corresponds to a throw on a fault plane, while the width of the embedded clay segment corresponds to the thickness of a clay sequence through which the fault develops. By performing several tests with different conditions (effective normal stress, maximum rotation, sand density, clay type, etc.) parameters may be varied to assess their effect on the development of the shear band and clay smear properties.

Early experimental studies dedicated to clay smear and shear band formation carried out at the Norwegian Geotechnical Institute (NGI) were performed in a classical geotechnical ring shear apparatus which allowed for large deformations, but was limited to low

stress levels equivalent to ca. 50 m burial under hydrostatic conditions (Sperrevik et al., 2000; Clausen and Gabrielsen, 2002; Kvaale, 2002).

More recently, a new ring shear apparatus was designed and constructed at NGI to investigate shear band formation and clay smear in unconsolidated sediments at greater burial depths (Torabi et al., 2007; Cuisiat et al., 2007). The new equipment allows for normal effective stresses up to 20 MPa, which correspond to a depth of ca. 2600 m under hydrostatic conditions or even higher in over-pressured reservoirs. These depth ranges cover the depth at which deformation (faulting) may have occurred for most North Sea reservoirs. In the absence of carbonate cementation, North Sea sediments remain loosely cemented until depths of 2.5–3 km until diagenesis takes place (Björlykke and Höeg, 1997).

In the new ring shear apparatus, the flow resistance and permeability can be measured across the specimen through 48 drainage points evenly distributed around the upper and lower rings (Fig. 2 left) during testing. The possibility of running permeability tests across the sheared specimen greatly improves the quantification of the sealing potential of clay smear and other deformation processes, and how this potential varies with normal stresses and shear displacement (i.e. fault offset) for different sediment types.

The main motivation of the work described in this paper is to pursue the experimental work initiated earlier (Cuisiat et al., 2007; Torabi et al., 2007) in order to increase our database of fault properties. The work focuses on the mechanisms associated with clay smear along faults in uncemented sediments as well as the associated permeability changes. The final aim is to develop an experimental database for quantification of fault texture, petrophysical properties, deformation and strength, and fluid flow properties of faults in unconsolidated sediments.

2. Clay smears: observation and prediction

Experimental studies (Weber et al., 1978; Sperrevik et al., 2000; Clausen and Gabrielsen, 2002; Karakouzian and Hudyma, 2002) as well as outcrop studies of clay smears in loose sandstone-shale sequences (Weber et al., 1978; Lehner and Pilaar, 1997; Doughty, 2003), and lithified sandstone–shale sequences (Lindsay et al., 1993), suggest that clay smearing is strongly dependent on the original thickness of the shale beds, the competency contrast between the shale and non-shale lithologies, the effective stress (i.e. burial depth), and the magnitudes and rates of faulting. Thick and weak source beds produce the thickest smears.

Conceptual models based on simple mechanical considerations have been used to explain clay smearing (Lehner and Pilaar, 1997; Mandl, 2000; Koledoye et al., 2003), and no mechanics-based predictive tool is yet available to model the processes associated with clay smear due to the difficulties associated with the complexity of the mechanisms (strain localisation, large displacement, extrusion, loading rates). Recent developments include the work by Gudehus and Karcher (2007) using hypoplasticity, and Cardozo and Cuisiat (2008) on fault-propagation folding in stratified media.

Practical predictive models are usually empirically based, by relating the potential for clay smearing to properties easily measured in well logs and seismic sections, such as amount of shale and fault throw across the sedimentary sequence (Yielding et al., 1997). The most common ones are the clay smearing potential (CSP, Bouvier et al., 1989), shale smear factor (SSF, Lindsay et al., 1993), and shale gouge ratio (SGR, Yielding et al., 1997).

- The clay smear potential (CSP) (Bouvier et al., 1989) is given by $CSP = c(T_c^2/d)$ where T_c is the thickness of the clay source bed,
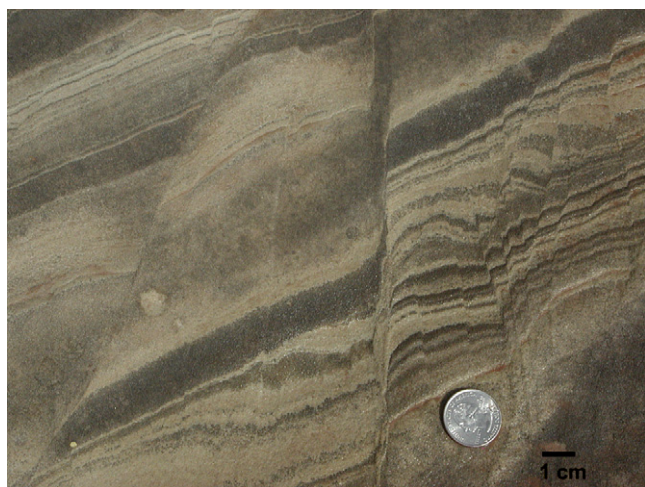

Fig. 1. Deformation bands in sandstone formation on the east side of Courthouse Canyon, Utah. Early soft-sediment deformation without cataclasis. Coin size is about 2 cm in diameter.
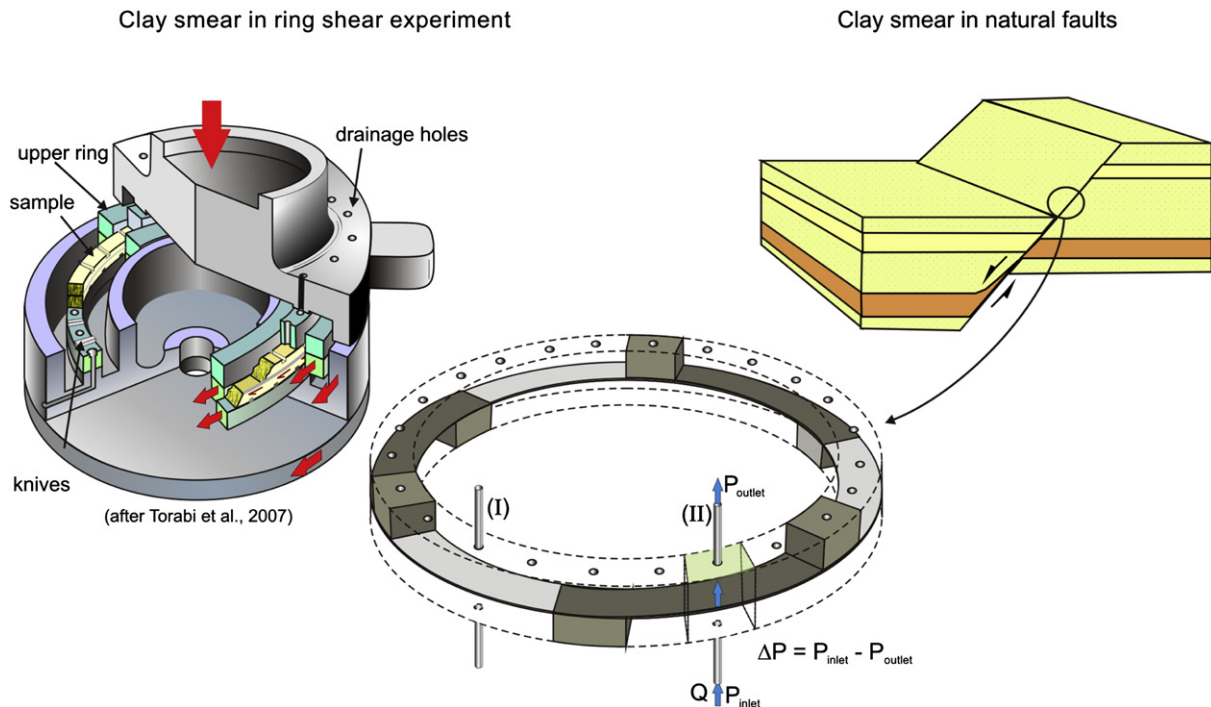
Clay smear in ring shear experiment   Clay smear in natural faults

Fig. 2. Use of ring shear device as an analogue to clay smear development during fault formation. Right: conceptual fault with clay smear. Middle: configuration of sand and clay segments in ring shear experiments described in this paper. Permeability measurements across shear band (I) and clay smear (II) are illustrated. Left: ring shear cell filled with sand (front part is omitted for clarity), after Torabi et al. (2007). Inner ring and outer ring diameters are equal to 25.4 and 30.48 cm, respectively. Moving parts are shown with red arrows.

d is the distance from the source bed, and c is a constant that needs to be calibrated. The clay smear thickness can be expected to correlate with CSP as shown by mechanical considerations (Egholm et al., 2008).

- The shale smear factor (SSF) (Lindsay et al., 1993) is the fault throw t divided by the vertical thickness of the offset shale source layer d_{cl}, i.e. SSF $= t/d_{cl}$.
- The shale gouge ratio (SGR) (Yielding et al., 1997) is the net clay percentage in the slipped interval, i.e. SGR $= \frac{\sum (V_{cl} \times \Delta z)}{t} \times 100\%$ where t is the local throw of the fault and V_{cl} is the clay volume factor in every interval Δz along the fault.

The previous parameters should be calibrated against well and outcrop data that document fault sealing. Based on an outcrop study of small faults in sandstone–shale sequence (with typical throws less than 1 m), Lindsay et al. (1993) concluded that with SSF less or equal to 7 continuous shale smears are expected, and with SSF less or equal to 11 continuous shale smears are probable. Faerseth (2006) found that continuous smear along large faults can develop when the shale smear factor (SSF), given by the fault throw divided by the thickness of the shale source layer, is less or equal to 4. However, smaller faults (sub-seismic) may exhibit a continuous smear for much higher smear factors, and display a greater variation in SSF (in the range of 1–50) compared to larger faults. Yielding et al. (1997) define an SGR limit of 15–20% between sealing and non-sealing faults, based on observations of pressure data across faults from wells in various tectonic settings. Bense and Van Balen (2004) obtained reasonable agreement of fault zone hydraulic conductivity inferred the SGR approach, and independently from calibrated numerical groundwater flow models.

Fault permeability–SGR relationships have been proposed for the North Sea based on well datasets (Manzocchi et al., 1999; Sperrevik et al., 2002). Other approaches are based on extensive experimental datasets from triaxial experiments, and usually relate fault permeability to strain or porosity (e.g. Crawford et al., 2002; Takahashi, 2003). However, the experiments are limited in terms of maximum fault displacement that can be reproduced.

3. Laboratory experiments on clay smear formation

3.1. Sand and clay used for testing

The sand used in the experiments is Baskarp sand No 15, a Holocene deposit from Vätteren (Sweden) which consists of more than 90% of angular to sub-angular well sorted quartz grains. The sand is fine to medium grained (60% passing diameter $D_{60} = 0.17$ mm). The unit weight of grains γ_s is equal to 26.0 kN/m³. The maximum and minimum dry unit weights γ_{dmax} and γ_{dmin} are equal to 16.86 kN/m³ and 14.28 kN/m³, respectively.

The clay used for the experiments is from the Troll field offshore Norway. The clay was sampled as part of a soil investigation program for the Troll field. Specimens from Unit I, 0–6 m depth were selected for testing (Lunne et al., 2007). The geomaterial is described as a very soft to firm, high plasticity and slightly over-consolidated clay. Unit I is a glacio-marine sediment deposited immediately after the de-glaciation of the area. Its deposition is thought to have occurred in a low energy marine environment while the sea level increased and water became deeper. The average percentage of clay fraction (<2 μm) for Unit I is 44% and the average percentage sand fraction (>60 μm) is 3%. The plasticity index is on average circa 37%. The unit weight of solid particles γ_s is equal to 26.8 kN/m³. The clay mineralogy is given in Table 1.

Before use in the ring shear apparatus, the Troll clay was consolidated uniaxially up to 1.5 MPa effective vertical stress. After unloading, the clay was then cut in segments shaped to fit within the confining rings of the ring shear apparatus. The water content w_c of the clay after compaction was measured to 26% giving an

Table 1
Mineralogy of the Troll clay from X-ray diffraction analyses (from Lunne et al., 2007).

Mineral	% Clay fraction (<2 μm)	% Sand fraction (>60 μm)
Illite	54	–
Kaolinite	19	–
Smectite	13	–
Chlorite	6	10
Quartz	2	65
Feldspar	2	17
Calcite	Minor	–
Pyrite	–	8

Table 3
Strength data from ring shear experiments. The depth of burial at time of faulting is estimated from peak stress and a pore pressure gradient of 10 MPa/km.

Test	Effective normal stress (MPa)	Peak shear stress (MPa)	Depth of burial at faulting (m)
RT15	3.5	2.20	570
RT16	0.7	0.79	149
RT17	7	3.90	1090
RT18	10.5	5.32	1582
RT19	3.5	2.19	569
RT20	10.5–3.5	2.46	596

initial porosity n_c of 41%. The compaction behaviour of the Troll clay as well as the time required for consolidation is investigated in an oedometer cell in which the permeability can be continuously interpreted from the excess pore pressure at the undrained bottom of the specimen (Sandbækken et al., 1986). The permeability of the clay at 3.5 MPa effective vertical stress (in oedometer conditions) is roughly equal to 0.0025 mD.

3.2. Description of the high stress ring shear apparatus

A brief description of the ring shear cell is given here. The reader is referred to Cuisiat et al. (2007) and Torabi et al. (2007) for more information about the apparatus.

In the ring shear cell, the sample is contained within the annular space created between the inner and outer confining rings, and the lower and upper rings (Fig. 2 left). The width of the annular space between the rings is 25.4 mm, and the maximum height of the sample is 44 mm, which is limited by the overlap required to hydraulically seal the gap between the upper ring and the confining rings. The inner and outer diameters of the confining rings are equal to 25.4 cm and 30.48 cm, respectively, giving a horizontal cross-sectional area of the sample equal to 223 cm². On the upper and lower rings 48 knives (or grooves) are evenly distributed to ensure transfer of the torque into the specimen. 48 orifices are evenly distributed between the knives on the upper and lower rings for flow measurements. During shearing, the upper ring is fixed and only the lower ring rotates clockwise. Two reaction arms on the upper frame provide the reaction forces against the rotation forces of the lower assembly. Two load cells measure the reaction forces, which in the absence of friction, sum to the shear forces exerted on the specimen. The effective normal stress onto the specimen is provided by a rigid loading frame. The normal displacement is calculated from an average of the sample height measured at 3 positions around the ring from three external linear variable displacement transducers.

The porosity is calculated from the total volume and pore volume based on the mass and dried densities of clay and sand. The total volume is updated during an experiment from the measured normal displacements. The porosity changes are calculated by assuming no volumetric deformation in the clay.

Table 2
Laboratory program for experiments dedicated to clay smear.

Test	Effective normal stress (MPa)	Over-consolidation	Burial depth[a] (m)
RT15	3.5	Normally consolidated	500
RT16	0.7	Normally consolidated	100
RT17	7	Normally consolidated	1000
RT18	10.5	Normally consolidated	1500
RT19	3.5	Normally consolidated	500
RT20	3.5–10.5	Overconsolidated	max 1500

[a] Estimated before testing.

3.3. Estimation of burial depth at time of failure

After initial normal loading and consolidation of the sample and prior to shearing, a K_o condition prevails in the sample. The major and minor effective principal stresses correspond to the vertical and horizontal effective stresses, respectively. During shearing, the sample is loaded to failure by imposing horizontal displacements and shear stresses, which results in a rotation and change in magnitude of the principal stresses, while the normal effective stress remains constant.[1] At failure assuming no volumetric deformation, the rotation reaches $45°$ and vertical and horizontal stresses are then equal. The horizontal direction is the direction of maximum shear stresses in the sample (Nowacki, 1967), and the maximum principal stress σ'_1 is inclined at $45°$ from the maximum shear direction, as observed experimentally by Mandl et al. (1977).

In a sedimentary basin, under no lateral constraints, normal faulting occurs as the Mohr-Coulomb slip (i.e. first Riedel shears) at an angle $45° - (\phi/2)$ from σ'_1. The major principal effective stress σ'_1 is the vertical overburden stress σ'_v in a basin under tectonic extension, which can be converted to a depth of faulting assuming a lithostatic gradient for the basin.

In the design of the experiments, we assume an effective lithostatic gradient of 10 MPa/km and a friction angle of 30° to calculate the normal stress to be applied so that failure occurs approximately at a given burial depth. The actual depth of faulting is back-calculated after the experiments from the measured stresses at peak condition.

3.4. Test description

The experiments are described in Table 2. After mounting and saturation inside the ring shear cell, the samples are first consolidated to nominal vertical stresses. A small cycling load (100 cycles, 5 kN amplitude) is used during normal loading to ensure good contact between the sample and the knives in the ring shear device. After consolidation, the samples are sheared under constant effective normal stress with a prescribed rotation velocity of 1 deg/5 min for a total length of 90 degrees (220 mm shear displacement). The velocity has been chosen such that the estimated pore pressure build-up at mid-height of the sample is negligible.

The permeability between two opposite openings across clay smear and sand–sand juxtaposition is measured during normal loading and every 15–30 degrees of shear rotation by imposing a flow rate Q at the injection point and a constant pressure at the outlet, and recording the pressure difference ΔP between inlet and outlet after steady state conditions are reached. Note that shearing is stopped during permeability measurements. Typically for measuring permeability across the clay smear, two opposite openings at the center of the fault throw are used, while the

---
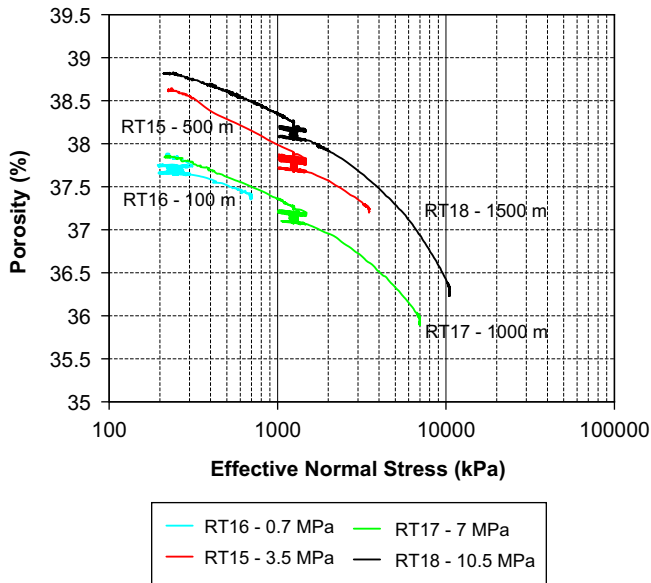
[1] This condition could differ in other experiments.

Fig. 3. Porosity changes during normal loading for clay smear tests. The corresponding (estimated) burial depths are: 100 m (RT16), 500 m (RT15), 1000 m (RT17), 1500 m (RT18).

remaining openings are closed. The interpreted coefficient of permeability is an average value of the sample containing undeformed sand, shear band, and clay smear. The permeability of the sample can be back-calculated using Darcy's law if one assumes that the flow is one dimensional and that the involved flow cross section is known, through the equation:

$$k = \frac{Q\mu}{A\left(\frac{\Delta P}{H}\right)} \tag{1}$$

where:

Q constant flow rate across sample (m^3/s)
ΔP pressure difference from inlet to outlet (Pa)
k permeability (m^2)
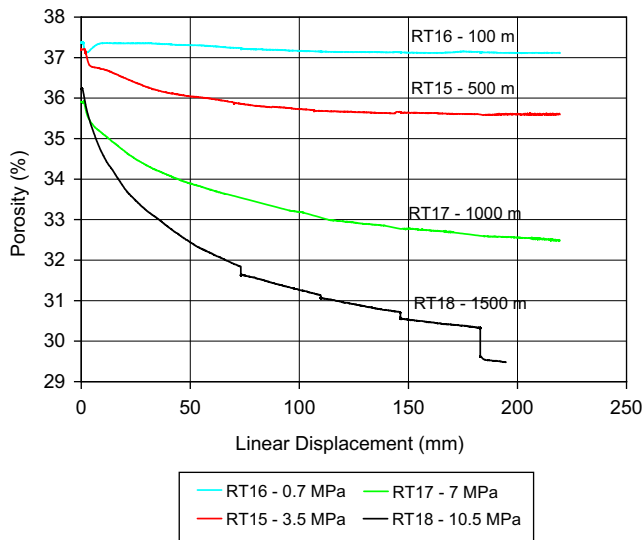μ fluid viscosity (10^{-3} Pa s, water)

Fig. 4. Porosity changes during shearing for clay smear tests. The corresponding (estimated) burial depths at the time of faulting are: 100 m (RT16), 500 m (RT15), 1000 m (RT17), 1500 m (RT18). *X*-axis represents the linear displacement of the bottom ring (i.e. fault throw).

H sample height (m)
A assumed flow area (m^2).

In practise the permeability is expressed in mD using 10^{-15} m^2 ≈ 1mD. A constant flow rate Q equal to $2.3\,10^{-7}$ m^3/s is used resulting in typical values of pressure difference equal to 5–$8\,10^3$ Pa at steady state. Steady state flow conditions are achieved after two to three minutes.

The main uncertainty when using Darcy's law relates to the size of the flow area. In the following, we will assume that the flow area is equal to 1/24th of the ring area for the interpretation of the permeability experiments. Given that this assumption may only be an approximation in reality, 3D finite difference modelling was conducted of the flow conditions during a permeability test in the ring shear apparatus. The modelling shows that the flow area may be closer to the area of the clay smeared zone, depending on the contrast between clay and sand permeability.

In tests RT15–RT18, three segments of clay 120° apart from each other are used. In tests RT19 and RT20 5 segments are used, 3 of them being only separated 15° from each other to address the formation of composite smear. One segment had only half the width of the others to study the effect of clay source thickness. The last segment serves as reference. In test RT20 the same configuration as test RT19 is used except that the clay is overconsolidated during shearing, i.e. shearing takes place at a normal stress level lower than the maximum experienced by the clay during normal loading. Samples for thin section analysis were taken after each ring shear test.

4. Results from experiments

4.1. Effect of effective normal stress

The development of fault deformation products for different effective normal stresses (i.e. simulating different burial depths) is investigated through tests RT15–RT18, which were performed under normal effective stress varying between 0.7 MPa and 10.5 MPa (i.e. estimated burial depth varying between 100 m and 1500 m). A corresponding depth of burial at time of faulting is inferred from peak stress conditions and a hydrostatic pore pressure gradient. The inferred depth of burial is close to the estimated one (Table 3).

The porosity changes during normal loading (i.e. burial of the sediments) and shear loading (i.e. faulting) are shown in Fig. 3 and Fig. 4, respectively. The normal loading curves show small porosity variations from test to test, but the normal stiffness of the samples is fairly similar for all tests especially after initial cyclic loading (around 1000 kPa) indicating reasonable repeatability of the preparation procedure of the samples.

Porosity loss increases with normal loading and shear displacement due to a combination of grain rolling, packing and crushing. The amount of porosity reduction during shearing clearly increases with normal loading. Test RT18 (1500 m estimated burial depth) shows important porosity reduction due to massive grain crushing. Note that this mechanism is time dependent as shown by continuous porosity reduction (Fig. 4) and stress relaxation (Fig. 5) measured during phases where shearing was resumed (overnight or weekend). Steady state conditions (i.e. shearing under no volume changes) are achieved for most tests except at high effective normal stress for which shearing should have been pursued beyond 90 degrees.

The effect of effective normal stress on the shear strength and normalised shear strength (i.e. apparent friction) of the sample is shown in Fig. 5. The peak shear stress correlates well with the normal stress applied onto the sample. More ductile behaviour is shown as normal stress increases. Note that test RT16 exhibits
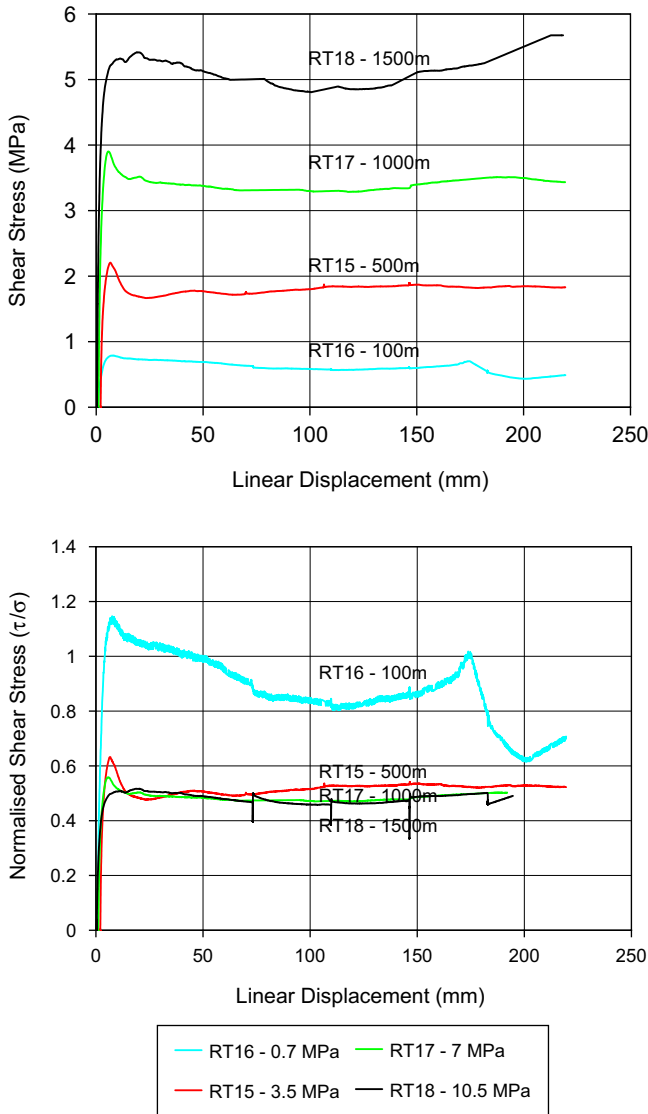
Fig. 5. Shear stress and normalised shear stress (i.e. ratio of shear stress over effective normal stress) versus linear displacement for clay smear tests. The corresponding (estimated) burial depths at the time of faulting are: 100 m (RT16), 500 m (RT15), 1000 m (RT17), 1500 m (RT18).

Fig. 6. Ratio of clay smear permeability k_{smear} over sand permeability before shearing $k_{sand,ini}$ versus linear displacement for clay smear tests. The corresponding (estimated) burial depths at the time of faulting are: 100 m (RT16), 500 m (RT15), 1000 m (RT17), 1500 m (RT18). Note that k_{smear} is equal to $k_{sand,ini}$ at zero rotation by convention (no smear).

permeability to initial sand permeability (at the end of consolidation) is shown versus linear displacement (220 mm = 90 degrees rotation) for different effective normal stresses. The initial sand permeability varies from test to test depending on initial packing and applied effective normal stress. For the reference case (RT15), the initial sand permeability is equal to 3350 mD at 3.5 MPa effective normal stress. For a given rotation in Fig. 6, the permeability might be an average value of different measurements taken at several locations along the smeared membrane. Note also that the permeability across the clay smears is in fact the average permeability across the whole specimen, in which several mechanisms might contribute to permeability reduction (grain rearrangement and grain crushing in the sand, clay smear). The tests show a dramatic permeability reduction with shearing, the reduction factor increasing with increasing effective normal stress. At higher normal stresses (e.g. RT17 and RT18) corresponding to greater depth of burial at the time of faulting, clay smear and sand–sand juxtaposition have similar permeability reductions for the same amount of shear (Fig. 7). Visual post-mortem observations of the sample (Fig. 8) show complex shear bands with occurrence of grain crushing not only in the sand–sand juxtaposition areas but also along the clay smear zone. Grain crushing might therefore be the dominant mechanism for permeability reduction at these depths. At lower effective normal stress (e.g. RT16) corresponding to shallow burial depth, the permeability across the clay smears is

abnormal high friction during shearing and two local peaks. This is probably caused by local failure at the knives due to low internal friction along the sidewalls within the ring cell. The low internal friction is a result of the low normal stress applied which is not suitable for the design of the high stress ring shear apparatus.

The residual friction angle, interpreted from the Coulomb failure criterion $\tau = \sigma' \cdot \tan \varphi$, gives a value around 25° for all tests, that is more or less independent of the stress level and of the presence of a clay smear. On the contrary, a similar clay smear experiment with kaolin showed lower shear strength for faulting with clay smear compared to a fault in pure sand only (Cuisiat et al., 2007), although the residual friction of illite is lower than that of kaolinite (e.g. Olson, 1974). The main reasons for the difference could be due to the presence of sand and silt in the natural clay tested in our experiments (circa 56%). The friction angle of a mixture of sand/silt and clay is well known to increase with the sand/silt content in the mixture (Lambe and Whitman, 1979).

The efficiency of clay smear in terms of permeability across the fault is illustrated in Fig. 6 where the ratio of clay smear
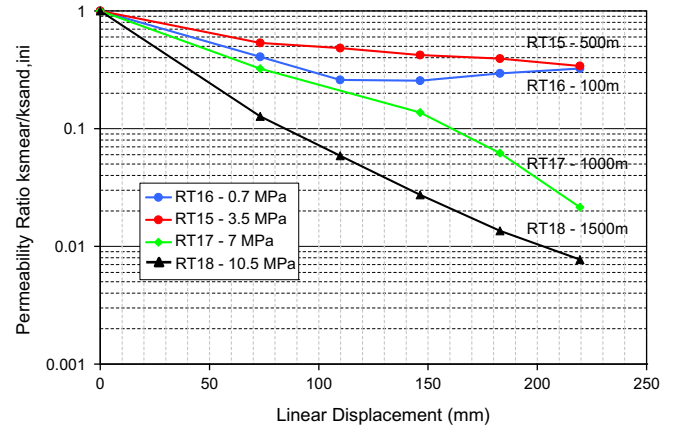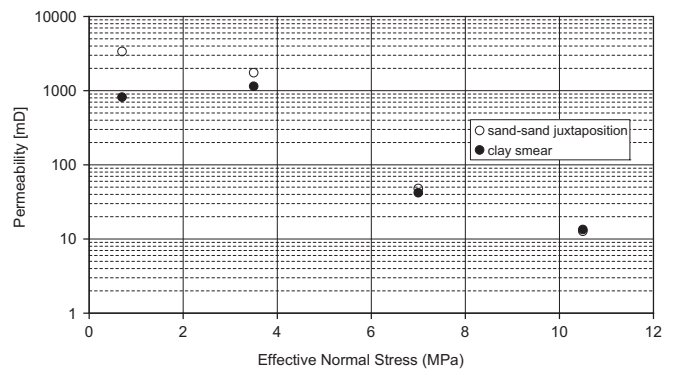

Fig. 7. Permeability across sand–sand juxtaposition k_{sand} and clay smear k_{smear} at the end of shearing (90°) versus imposed effective normal stress during shearing for all tests. The corresponding (estimated) burial depths at the time of faulting are: 100 m (RT16), 500 m (RT15), 1000 m (RT17), 1500 m (RT18).

much lower than in the sand–sand juxtaposition areas (Fig. 7). Given the visible absence of sand shear (Fig. 8), clay smear seems to be the main permeability-reducing mechanism for faults formed at low burial depth. The contrast between permeability across clay smears and sand – sand juxtaposition clearly decreases with increasing applied effective normal stress (Fig. 7).

The geometrical characteristics (i.e. thickness, continuity, waviness) of the clay smears are qualitatively observed after testing by removing progressively the sand–clay material within the ring cell. Clay smears show local buckling and variation in clay smear thickness at low effective normal stress (0.7 MPa), see Fig. 8 (top). At higher normal stresses (3.5, 7 and 10.5 MPa), clay smear occurs within wider deformation bands where grain rolling and/or grain crushing takes place. The thickness of the combined zone of clay smear and sand shear seems to increase with effective normal stress. Continuity of the clay smear is observed in all cases after dismounting the sample, except for high normal stress (RT18) where a local rupture of the clay smear is seen. The "puncture" cannot be obviously correlated to changes in permeability measurements. Thin sections taken from the samples were used to qualitatively describe the amount of grain flaking/splitting during

deformation (Fig. 8, bottom). The quality of the thin sections is variable because of the difficulty to saturate the clay-rich zone with epoxy. Nevertheless, it can be seen that the degree of grain crushing is increasing with increasing normal stress. At low effective normal stress, mixing of clay and sand grains is observed with diffuse boundary between clay smear and sand. At higher normal stress, sharper transitions are observed with pronounced grain comminution within or along the clay smear. In the zone along the clay smear, sand grains are floating in a matrix of crushed material.

A significant amount of sand grains floating in the clay smear can contribute to increase significantly the permeability of the clay membrane, compared to the permeability of a membrane made of pure clay. Indeed the permeability of the clay smear, which is at the most two orders of magnitude lower than the initial permeability of the sand (Fig. 6), is much higher than the permeability of a pure Troll clay sample tested in an oedometer cell (Section 3.1).

4.2. Influence of clay source thickness and multiple clay layers

In tests RT19 and RT20, five clay segments are embedded into the sand to investigate the effect of overlapping clay smear and clay
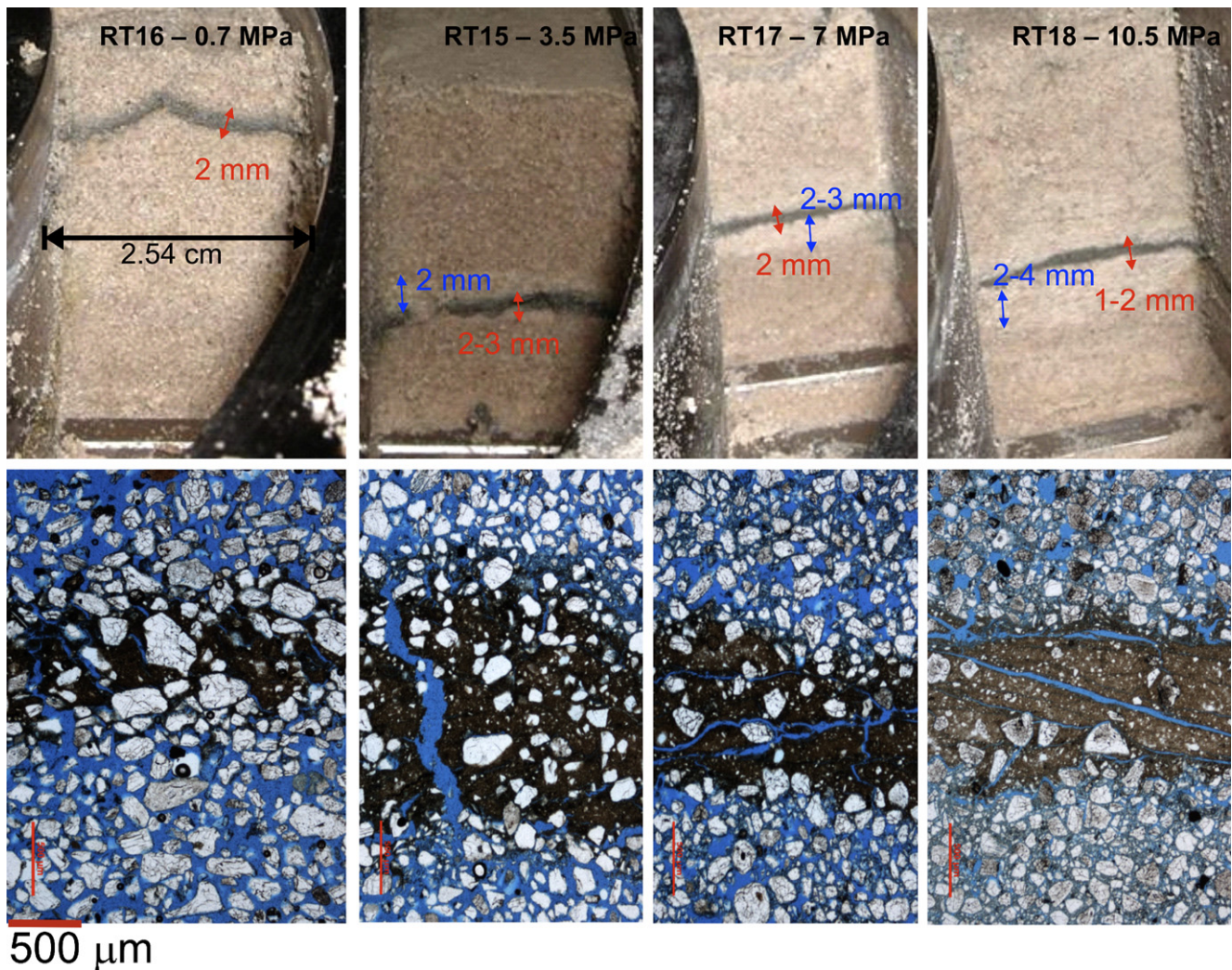

Fig. 8. Vertical cross-sections of clay smear at the end of testing. The cross-sections are taken normal to shear direction in between upper and lower clay segments. Top: Photographs during dismounting of sample. Bottom: Corresponding thin sections. Sample width in top figure is 2.54 cm, scale for thin sections is 500 μm. Note that the thin fractures across and along the smear in thin sections of tests RT15, RT17 and RT18 are probably induced during the preparation of the thin sections. Apparent rupture on RT15 (top figure) is due to loose grains during dismounting of sample. The corresponding (estimated) burial depths at the time of faulting are: 100 m (RT16), 500 m (RT15), 1000 m (RT17), 1500 m (RT18).
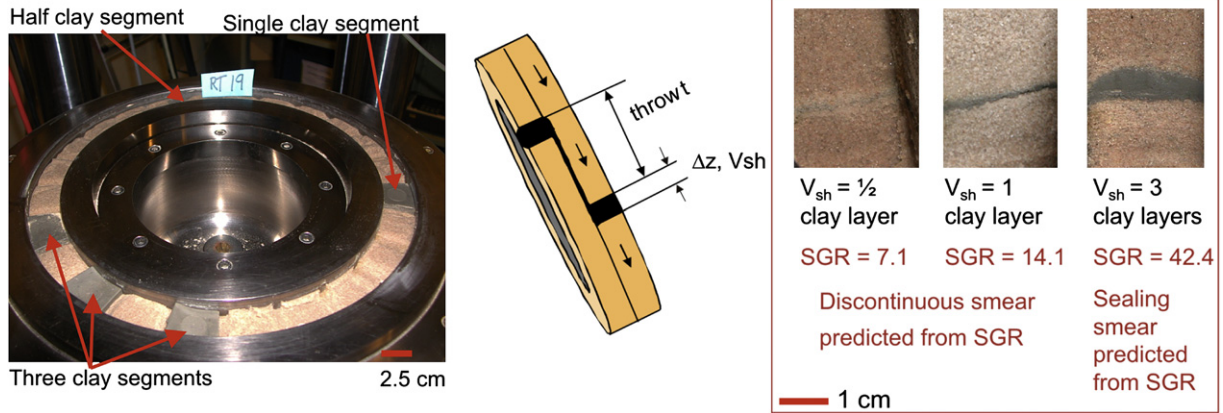
Fig. 9. Effect of clay thickness and composite smear. Shearing at 3.5 MPa effective normal stress (estimated burial depth at the time of faulting of 500 m). Left: Position of clay segments in tests RT19 and RT20. Photograph width approximately 25.4 cm. Right: Cross-sections through clay smear at end of shearing for test RT19. Photograph width approximately 2.54 cm.

segment thickness within one test (Fig. 9, left). Three segments are 30° apart from each other to overlap during rotation of the ring. One segment has half the thickness of the others, the last one is for reference. In test RT20, the same configuration is used, but the sample is first normally loaded up to 10.5 MPa, and then unloaded to 3.5 MPa to simulate burial and uplifting before faulting. As a result, the clay and sand are in an "over-consolidated" state. Both specimens RT19 and RT20 are sheared under a constant effective normal stress of 3.5 MPa equivalent to a burial depth of 500 m.

Continuous clay smear is observed for both tests in all segments except for the segment with half thickness in test RT19 where a visible smear rupture circa 5 cm long is observed (Fig. 9 right). In this case, only a very diffuse clay smear band, filling the pore space between sand grains is observed (Fig. 10). The thickness of the clay smear seems to increase and the transition between clay smear and sand grains is more distinct when the thickness of the clay segment increases, although zones with complete mixing of sand and clay still remain. A 7 mm thick composite smear is observed for the
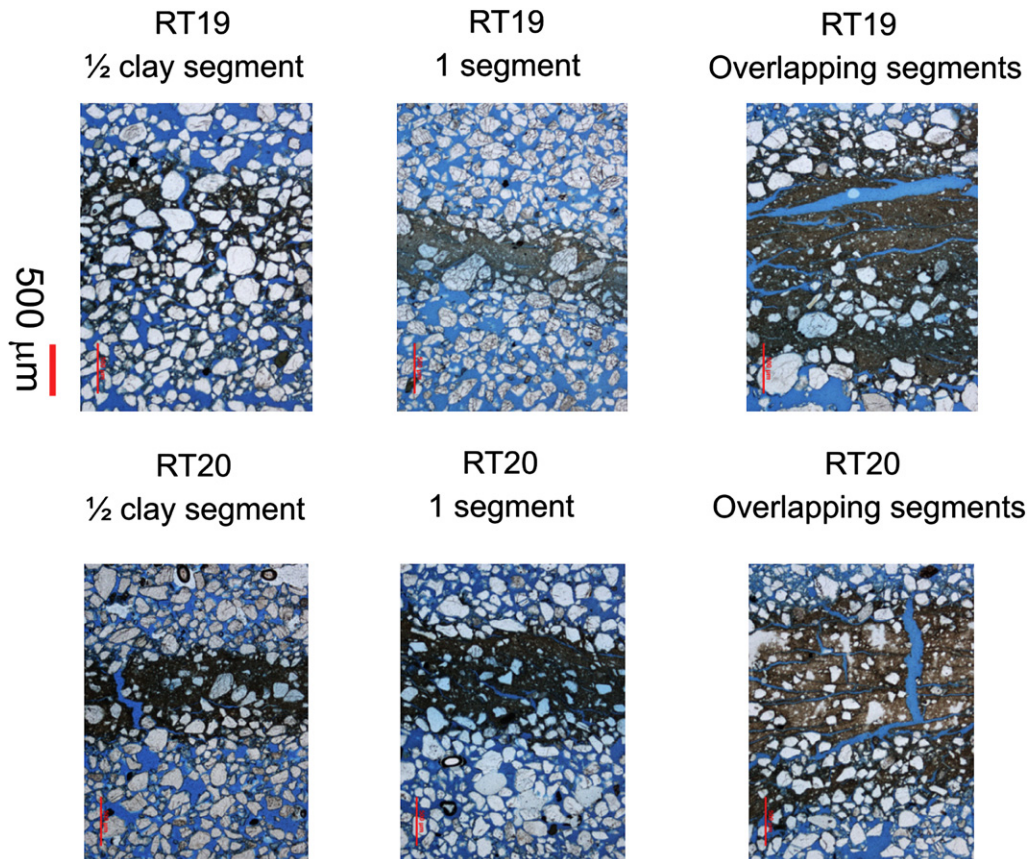

Fig. 10. Thin sections from tests RT19 (normally consolidated) and RT20 (over-consolidated). Shearing at 3.5 MPa effective normal stress (estimated burial depth at the time of faulting of 500 m). Note that the thin fractures observed in tests RT19 and RT20 are probably induced during the preparation of the thin sections.

overlapping clay segments, with clay issued from more than one clay segment as indicated by embedded thin layers of sand within the smear (Fig. 11). Sand shear is seen to a certain degree for all segments (grain rolling or crushing), but seems to be more developed when the amount of clay available for smearing decreases. Sand shear is also more developed in the over-consolidated sample (RT20).

When clay segments overlap, a sand wedge can form between the smear and the clay segment (Fig. 12). The resulting thick clay smear is clearly visible with a marked layered structure of inter-bedded clay/sand rich zones. The impact of overlapping segments is clearly visible from the overall stress-displacement response (Fig. 13). Tests RT15 and RT19 show very similar behaviour until circa 110 mm linear displacement (i.e. 45° rotation), which corresponds to onset of clay overlap in test RT19. Whereas the shear strength of RT15 remains more or less constant with increasing displacement, the shear strength of RT19 increases with linear displacement, due to increased shear resistance with increasing overlapping area. A similar behaviour is obtained for RT20, except that the shear strength is generally higher because the sample is over-consolidated. Note also a more brittle behaviour in test RT20 at the early stage of shearing, compared to RT19.

The results from permeability measurements show a higher permeability of composite smear than for smear issued from a single segment by the same ring rotation (see "RT19 – 3 clay segments" compared to "RT19 – 1 clay segment" in Fig. 14). Further, the permeability of composite smears does not decrease monotonously with increased ring rotation. After a ring rotation of 60° (circa 145 mm linear displacement), the permeability increases most probably due to the formation of interbedded sand wedges between the smears with higher permeability than the smeared clay. Note also that the permeability of the clay smear developed from half a clay segment ("RT19 – ½ clay segment" in Fig. 14) is slightly higher than the permeability of the smear for a full segment ("RT19 – 1 clay segment"). Since a constant cross-flow area is assumed in the interpretation of permeability Eq. (1), this could indicate a larger amount of sand mix within the smear for a thinner clay source. However, this result should be taken with caution as the interpreted permeability depends highly on the value of the

cross-flow area used. If the true flow area is rather proportional to the length of the smear membrane, for the same conditions of rotation, flow rate and pressure gradient, the ratio between the permeability of half a clay segment and that of a full segment is then equal to $(l - w)/(l - w/2)$, where l is the linear (shear) displacement and w the width of the clay segment. This ratio increases from 0.65 after 60 mm linear displacement to 0.93 after 225 mm.

The effect of over-consolidation is clearly shown in Test RT20: the permeability across the smear for the over-consolidated specimen (RT20) is lower than for the case of a normally consolidated specimen (RT19) independently of segment thickness (Fig. 14).

5. Discussion

5.1. Conditions for clay smear formation

The kinematics and mechanics of clay smear remain poorly understood. Outcrop field studies (Lindsay et al., 1993; Lehner and Pilaar, 1997; van der Zee and Urai, 2005; Bense et al., 2003) indicate that clay smear develops from a combination of lateral clay injection and clay abrasion within the shear zone. Lehner and Pilaar (1997) suggested that fault smear relates to pull-apart mechanics creating normal fault relay zones across the shale beds, thereby forming an extensional releasing bend. Egholm et al. (2008), from discrete element modelling of fault zone evolution in a granular material, show that contractional bends were more likely to be the driving forces for clay smear. In our experiments, because of the stress configuration inherent to the ring shear apparatus, it is likely that abrasion smear is the dominant mechanism for clay smearing. This is in line with the observed constant thickness of the smear along the fault. In particular the thickness of the smear does not seem to increase close to the clay segments.

Shear deformation in normally consolidated sediments results in compaction and strain hardening due to interlocking of the crushed grains, which may promote the spread of deformation into adjacent sediments (Rawling and Goodwin, 2006). In the ring shear apparatus this is hampered by the limited sample size. Nevertheless, the grain size distribution of deformation bands induced in the
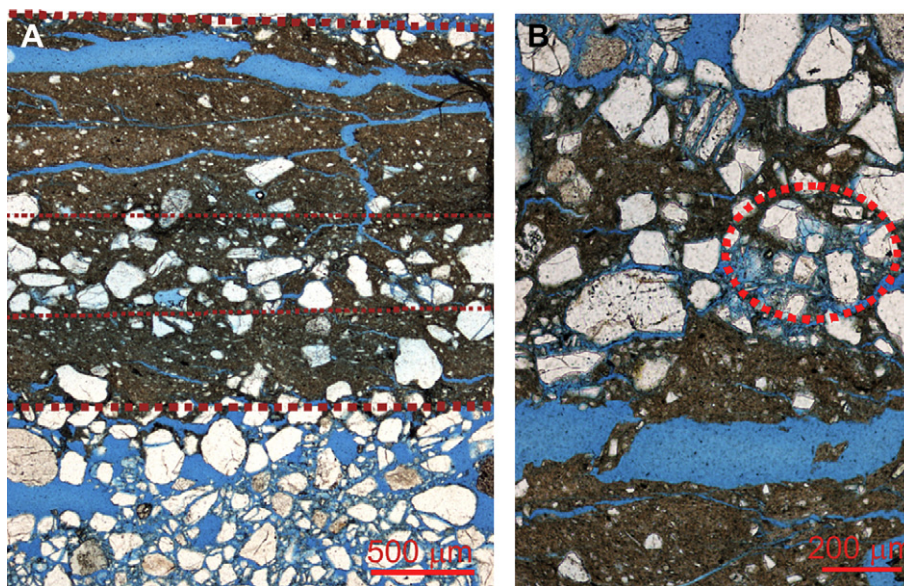

Fig. 11. Thin sections from overlapping clay layer in RT19. Shearing at 3.5 MPa effective normal stress (estimated burial depth at the time of faulting of 500 m). (A) Layer enriched with sand within the clay smear and (B) lens of crushed sand within the clay smear. Note that the thin fractures observed are probably induced during the preparation of the thin sections.
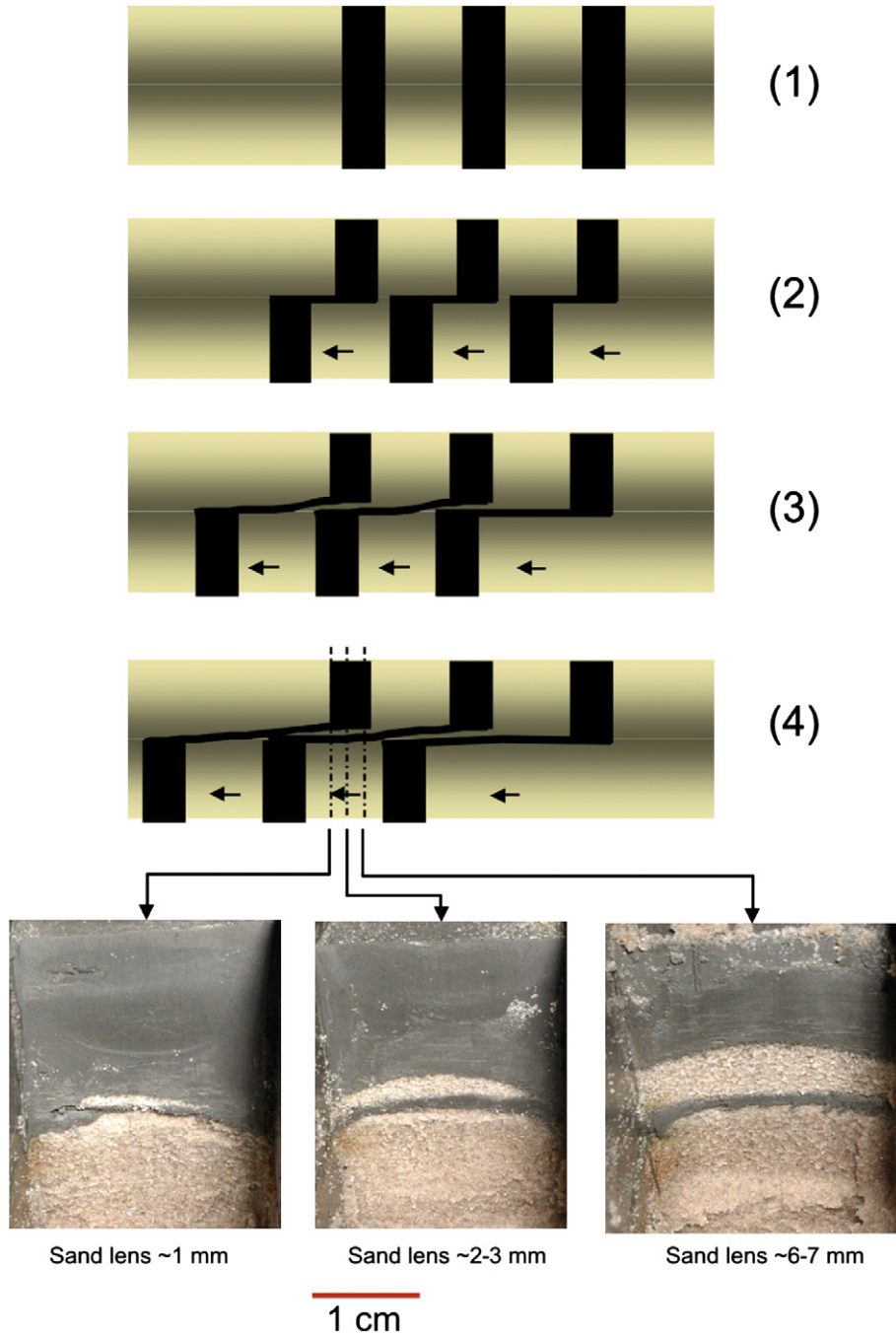
Fig. 12. Sketch showing formation of sand wedge during faulting in clay–sand layered sediments, and observed cross-sections at end of shearing in test RT19. Shearing at 3.5 MPa effective normal stress (estimated burial depth at the time of faulting of 500 m). All sections are within 5 cm along the shear direction. The sand wedge thins in the direction of rotation of the lower ring. Photograph width approximately equal to 2.54 cm.

ring shear apparatus is comparable to that of natural deformed sands under similar burial conditions (Torabi et al., 2007).

5.2. Clay smear permeability from smear thickness

The clay smear permeability values interpreted from the ring shear tests refer to average permeability values over the whole height of the sample, i.e. of the underformed sand, the deformed sand and the clay smear. In the following, we estimate the permeability of the clay smear alone from a simple permeability model. It is assumed that an average permeability can be defined for the clay smear and the sand separately.

The average permeability k_{avg} normal to a stratified medium made of sand and clay smear is calculated from the harmonic average:

$$\frac{k_{avg}}{k_{sand}} = \frac{1}{1 + \frac{k_{sand}}{k_{smear}}\frac{t_{smear}}{t_{tot}} - \frac{t_{smear}}{t_{tot}}} \qquad (2)$$

where:

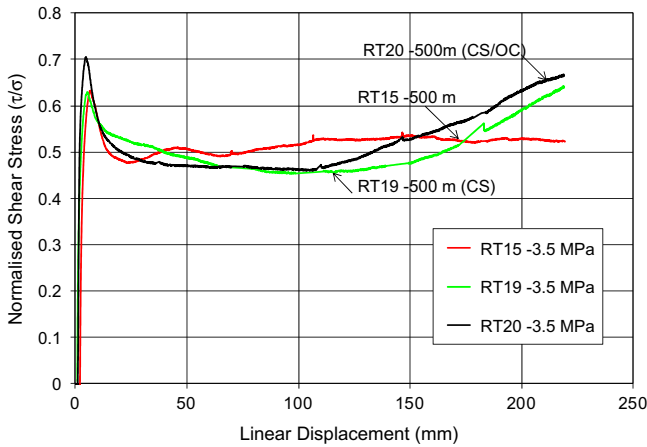|	
k_{smear}	is the permeability of the clay smear
k_{sand}	is the permeability of the sand
t_{tot}	is the total height of the sample
t_{smear}	is the thickness of the clay smear.

Fig. 13. Normalised shear stress versus linear displacement for tests RT15, RT19 (composite smear CS) and RT20 (composite smear and over-consolidated CS/OC). All tests are sheared under 3.5 MPa effective normal stress.

The permeability ratio k_{avg}/k_{sand} is plotted in Fig. 15 for different values of k_{sand}/k_{smear}, i.e. ratio between sand and clay smear permeability. The results from the ring shear tests are plotted on the figure, based on the measured permeability at end of shearing (90° rotation) and clay smear thicknesses reported in Fig. 8. Relatively small contrasts between sand and clay smear permeability are back-calculated from the average permeability model, except at shallow burial depth (test RT16) for which the clay smear permeability is 100 times less than that of the sand. Thus, the model is consistent with the idea that at shallow depth, clay smear is more efficient than sand–sand juxtaposition.

Note also that the inferred permeability of the smear is much higher than that of pure clay measured in an oedometer cell (Section 3.1). Permeability increase during shearing can result from 1) clay dilatancy causing changes in the microstructure (Bolton and Maltman, 1998; Takizawa et al., 2005), 2) sand mixing in the clay membrane.
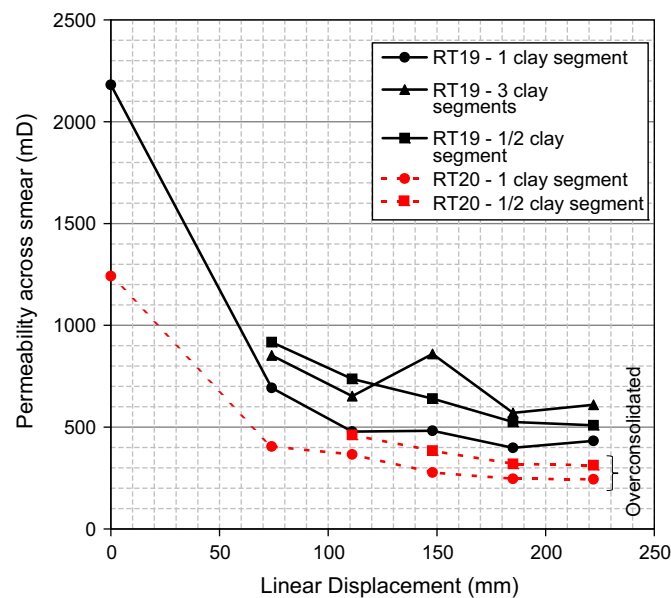

Fig. 14. Permeability across clay smear from single clay segment, half segment and three segments versus linear displacement in tests RT19 and RT20 (over-consolidated). Both tests are sheared under 3.5 MPa effective normal stress.
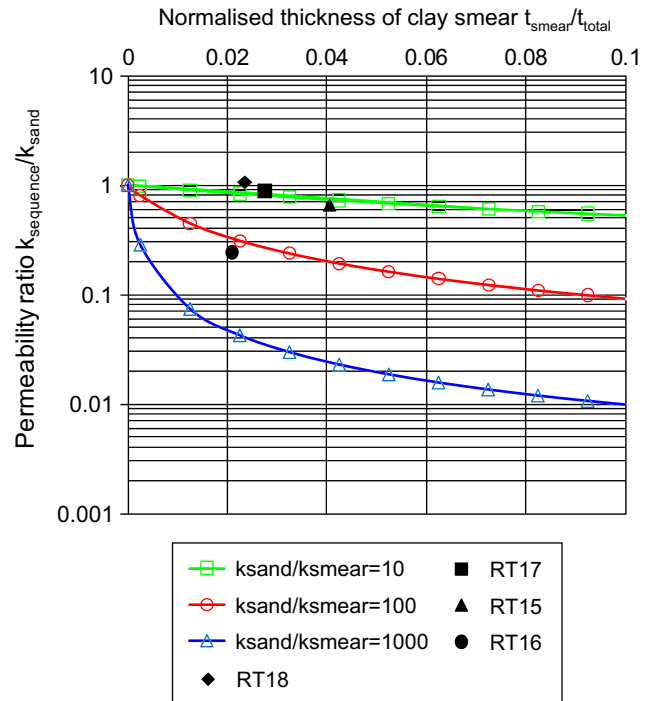

Fig. 15. Average permeability of sand–clay smear layer sequence (harmonic average) versus ratio of clay smear thickness to total thickness for different ratios of sand permeability k_{sand}/clay smear permeability k_{smear}. The ring shear tests are plotted with black filled symbols. The thickness of the clay smear is estimated after dismounting the samples (Fig. 8).

5.3. Comparison with empirical models

The efficiency of the developed clay smear to seal is assessed from the empirical parameters presented earlier. The parameters are calculated from the clay smear experiments in Table 4. In all experiments, clay smear occurs along the shear plane with some variation in clay smear thickness. Discontinuity in clay smear is

Table 4
Shale Smear Factor SSF, Clay Smear Potential CSP and Shale Gouge Ratio SGR calculated at mid-point along slipped interval from ring shear experiments on clay smear. Tests RT19, RT15 and RT20 are sheared under 3.5 MPa effective normal stress, but RT20 is over-consolidated. Tests RT16, RT17 and RT18 are sheared under 0.7, 7 and 10.5 MPa effective normal stress, respectively. The corresponding (estimated) burial depths at the time of faulting are: 100 m (RT16), 500 m (RT15, RT19, RT20), 1000 m (RT17), 1500 m (RT18).

	RT19, RT20	RT15–RT20	RT19, RT20
Throw (mm)	219.5	219.5	219.5
Clay segment thickness (mm)	15.5	31	31
Clay volume factor (%)	100	100	100
Number of clay segments	½ layer	1 layer	3 layers
Shale Smear Factor (SSF)	**14.2**	7.1	2.4
Clay Smear Potential (CSP)	1.1	4.4	39.4
Shale Gouge Ratio (SGR)	**7.1**	**14.1**	42.4
Thickness of smear (mm)	0.1–2	2–3	2–4 up to 7
Continuity of smear	Discontinuous (RT19) Continuous (RT20)	Continuous except at high burial depth (RT18)	Continuous

In bold figures: probable discontinuous smear predicted from empirical relationships.
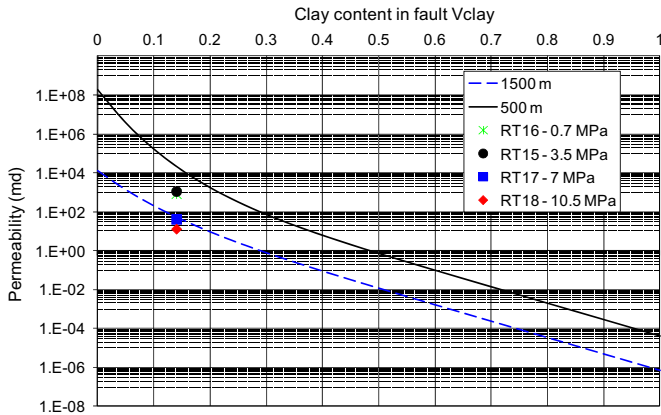
Fig. 16. Comparison of permeability data from ring shear tests (one clay segment) with empirical relationship proposed by Sperrevik et al. (2002). The clay content in the fault rock is taken equal to the SGR for the ring shear data. The corresponding (estimated) burial depths at the time of faulting are: 100 m (RT16), 500 m (RT15), 1000 m (RT17), 1500 m (RT18).

observed for test RT19 (half-segment width) in agreement with SSF and SGR estimations. For one clay segment, the values of SSF and SGR are close to the limit for breach of the smear (SSF = 7 and SGR = 14). Continuous smear is observed in all experiments, although a small 'puncture' is observed at high burial depth (1500 m, RT18).

The previous parameters do not provide quantitative relationship between smear development, rock properties, stress conditions and fluid flow properties. Takahashi (2003) for instance showed through laboratory experiments that a critical SSF for seal breach depends on the effective normal stress applied to the fault during smearing. Our experiments also indicate that the burial depth (or normal stress) might control the continuity of the smear. Nevertheless, our experiments are in agreement with field evidence showing a first order correlation between SGR and seal capacity (Naruk, 2008).

The results of the ring shear experiments are also compared to the empirical relationship proposed by Sperrevik et al. (2002) which relates fault rock permeability to maximum burial depth, depth at the time of faulting and clay content in fault rock. In Fig. 16, the empirical relationship is plotted for two values of maximum burial depth (same as depth at the time of faulting in this case) equal to 500 and 1500 m together with the permeability data from ring shear tests with one clay segment. The ring shear test results show a first order agreement with the empirical relationship of Sperrevik et al. (2002) based on data of nearly 100 normal faults from clastic reservoirs in the North Sea (Fig. 16).

5.4. Fault permeability reduction with increasing burial depth

Despite uncertainties related to the interpretation of flow measurements (in particular the flow area), the test results suggest that clay smear and shear displacements are the main permeability reduction mechanism for faults formed at low burial depths (Fig. 17). Sand–sand juxtaposition shear is dominated by grain rolling causing only minor permeability reduction. At greater depths grain crushing along the clay smear zone and in the sand–sand juxtaposition areas contributes as much to permeability reduction as the formation of a clay smear (Fig. 17). The transition between the two scenarios is likely to occur at around 500 m burial depth. At this depth, some grain crushing is observed in the experiments (e.g. test RT15), but not as developed as for experiments conducted at 1000 m and 1500 m burial. In general the burial depth at time of faulting has a larger influence on the estimated permeability change than the clay segment thickness and overconsolidation ratio, within the range of parameter variation investigated in the experiments.

6. Conclusions

In this paper, we have presented the results from experimental work carried out with a high stress ring shear apparatus to investigate mechanisms of clay smear along faults in uncemented sediments at various burial depths, and its impact on fluid flow properties. The experiments consist of shearing a ring of sand with embedded clay segments, thereby simulating faulting through a layered sand–clay sequence. Baskarp sand No 15 and a natural glacio-marine clay from the Troll field are used for testing. Visual inspection of the samples after testing, analyses of thin sections and permeability measurements across the shear zone are used to describe clay smear continuity, thickness and permeability.

Deformation processes such as grain reorientation, clay smear and cataclasis are identified from the tests. The complexity of the shear zone is observed to increase with greater burial depth at time of faulting. The experiments suggest that at shallow burial depth in clay-rich sediments, clay smear is the most efficient mechanism for permeability reduction. At this depth, sand–sand juxtaposition shear is dominated by grain rolling causing only minor permeability reduction. At greater burial depths, permeability reduction is dominated by grain crushing. Measurements of permeability both across clay smear and sand–sand juxtaposition yield similar values.

The observed thickness of clay smear is more sensitive to the thickness of the sheared clay layers than other parameters tested within the limited test program. Shearing of multiple clay layers (3 layers) produces a composite clay smear 2–3 times thicker than for a single clay layer, whereas when reducing the clay layer thickness to one half of the reference layer, a thin and discontinuous clay smear is produced. The permeability across the clay smear is found to increase as the thickness of the clay source decreases for single clay layers, but the permeability for composite smear is more complex and a clear trend is not found from the only two tests performed. Over-consolidation of the sample prior to shearing has no significant influence on the thickness and continuity of the clay smear produced, but a reduction in permeability both for clay smears and initial sand is found when compared to a normal
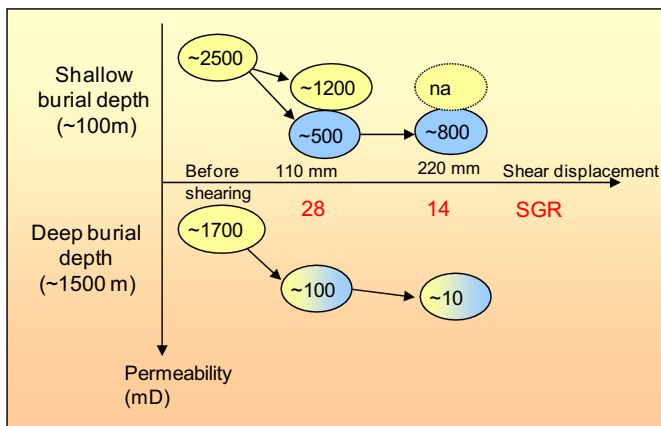

Fig. 17. Synthesis of permeability trends from ring shear experiments. Values indicate permeability in mD for clay smear (blue) and sand–sand juxtaposition (yellow) or a combination (yellow/blue). No flow measurement is available in the sand–sand juxtaposition for low effective normal stress (i.e. low burial depth) at end of shear. Ring shear displacements have been converted to shale gouge ratio (SGR). (For interpretation of the references to colour in this figure legend, the reader is referred to the web version of this article.)

consolidated test. This implies that the initial density of the material is important for the permeability measurements.

The results from the experiments show many similarities with field or outcrop natural observations. Next to clay smearing, drag or injection of clay sand along the fault plane also occurs. Due to mixing of clay and sand into the fault core, the flow properties of the fault are expected to be anisotropic with higher permeability along the shear direction (Bense and Van Balen, 2004). However, more experimental data should be collected in order to develop better trend lines and predictive models of fault properties. Field and outcrop observations could be used actively to constrain the experimental conditions to use in future tests. Future research will complement the existing dataset as well as address formation of phyllosilicate framework fault rocks in unclean sand with varying clay content, clay mineralogy, burial depth, and fault throw. More tests are also needed for improving the understanding of deformation bands in multiple clay layers and the effect of composite smear on fault permeability. Other types of experimental set-ups such as a biaxial plane strain apparatus (Rykkelid and Skurtveit, 2008) may also be used to reproduce more accurately the stress and strain conditions during basin extension and fault propagation through layered sand–clay sequences. Ultimately, through more extensive databases, models can be implemented into reservoir simulators to capture better the impact of faults on oil recovery (Jolley et al., 2007).

Acknowledgements

References

Annunziatellis, A., Beaubien, S.E., Bigi, S., Ciotoli, G., Coltella, M., Lombardi, S., 2008. Gas migration along fault systems and through the vadose zone in the Latera caldera (central Italy): implications for CO_2 geological storage. International Journal of Greenhouse Gas Control 2, 353–372.

Antonellini, M., Aydin, A., Pollard, D., 1994. Microstructure of deformation bands in porous sandstones at Arches National Park, Utah. Journal of Structural Geology 16, 941–959.

Bense, V., Van den Berg, E., Van Balen, R., 2003. Deformation mechanisms and hydraulic properties of fault zones in unconsolidated sediments; the Roer Valley rift system, The Netherlands. Hydrogeology Journal 11, 319–332.

Bense, V.F., Van Balen, R., 2004. The effect of fault relay and clay smearing on groundwater flowpatterns in the lower rhine embayment. Basin Research Volume 16, 397–411.

Bishop, A.W., Green, G.E., Garga, V.K., Andersen, A., Browns, J.D., 1971. A new ring shear apparatus and its application to the measurement of residual strength. Geotechnique 21, 273–328.

Björlykke, K., Höeg, K., 1997. Effects of burial diagenesis on stresses, compaction and fluid flow in sedimentary basins. Marine and Petroleum Geology 14, 267–276.

Bolton, A., Maltman, A., 1998. Fluid-flow pathways in actively deforming sediments: the role of pore fluid pressures and volume change. Marine and Petroleum Geology 15, 281–297.

Bouvier, J.D., Kaars-Sijpesteijn, C.H., Kluesner, D.F., Onyejekwe, C.C., Van der Pal, R.C., 1989. Three dimensional seismic interpretation and fault sealing investigations, Nun River field, Nigeria. AAPG Bulletin 73, 1397–1414.

Caine, J.S., Evans, J.P., Forster, C.B., 1996. Fault zone architecture and permeability structure. Geology 24, 1025–1028.

Cardozo, N., Cuisiat, F., 2008. Fault propagation folding modeling with FLAC. In: Proceedings of the 1st International FLAC/DEM Symposium on Numerical Modeling, 25–27 August 2008, Minneapolis, USA.

Chuhan, F.A., Kjeldstad, A., Bjorlykke, K., Hoeg, K., 2002. Porosity loss in sand by grain crushing – experimental evidence and relevance to reservoir quality. Marine and Petroleum Geology 19, 39–53.

Clausen, J.A., Gabrielsen, R.H., 2002. Parameters that control the development of clay smear at low stress states: an experimental study using ring shear apparatus. Journal of Structural Geology 24, 1569–1586.

Crawford, B.R., Myers, E.D., Woronov, A., Faulkner, D.R., Rutter, E.H., 2002. Porosity Permeability Relationships in Clay-bearing Fault Gouge. Society of Petroleum Engineers Inc. SPE/ISRM 78214, Rock Mechanics Conference, October 2002.

Cuisiat, F., Skurtveit, E., Cleave, R., 2007. Fault seal prediction in unconsolidated sediments with a novel experimental apparatus. In: Proceedings of the 7th ISRM Congress on Rock Mechanics, Lisboa, Portugal.

Doughty, P.T., 2003. Clay smear seals and fault sealing potential of an exhumed growth fault, Rio grande rift, new Mexico. American Association of Petroleum Geologists Bulletin 87, 427–444.

Egholm, D.L., Clausen, O.R., Sandiford, M., Kristensen, M.B., Korstgard, J.A., 2008. The mechanics of clay smearing along faults. Geology 36, 787–790.

Faerseth, R.B., 2006. Shale smear along large faults: continuity of smear and the fault seal capacity. Journal of the Geological Society 163, 741–751.

Fisher, Q.J., Knipe, R.J., 1998. Fault sealing processes in siliciclastic sediments. In: Jones, G., Fisher, Q., Knipe, R. (Eds.), Faults, Fault Sealing and Fluid Flow in Hydrocarbon Reservoirs. Geological Society of London, special publication, vol. 147, pp. 117–134.

Fisher, Q.J., Knipe, R.J., 2001. The permeability of faults within siliciclastic petroleum reservoirs of the north sea and Norwegian continental shelf. Marine and Petroleum Geology 18, 1063–1081.

Gudehus, G., Karcher, C., 2007. Hypoplastic simulations of normal faults without and with clay smears. Journal of Structural Geology 29, 530–540.

Hickman, S., Sibson, R.H., Bruhn, R., 1995. Introduction to special section: mechanical involvement of fluids in faulting. Journal of Geophysical Research 100, 12831–12840.

Hungr, O., Morgenstern, N.R., 1984. High velocity ring shear tests on sand. Geotechnique 34, 415–421.

Jolley, S.J., Dijk, H., Lamens, J.H., Fisher, Q.J., Manzocchi, T., Eikmans, H., Huang, Y., 2007. Faulting and fault sealing in production simulation models: Brent Province, northern North Sea. Petroleum Geoscience 13, 321–340.

Karakouzian, M., Hudyma, N., 2002. A new apparatus for analog modeling of clay smears. Journal of Structural Geology 24, 905–912.

Koledoye, B.A., Aydin, A., May, E., 2003. A new process-based methodology for analysis of shale smear along normal faults in the Niger Delta. American Association of Petroleum Geologists Bulletin 87, 445–463.

Kvaale, T., 2002. Et stadium av reservoarsand i ringskjærapparat for å simulere oppførselen i forkastningssoner. Master thesis, University of Oslo.

Lambe, T.W., Whitman, R.V., 1979. Soil Mechanics. John Wiley, New York.

Lehner, F.K., Pilaar, W.F., 1997. The emplacement of clay smears in synsedimentary normal faults: inferences from field observations near Frechen, Germany. In: Møller-Pedersen, P., Koestler, A.G. (Eds.), Hydrocarbon Seals: Importance for Exploration and Production. Norwegian Petroleum Society, Special Publication, vol. 7, pp. 39–50.

Lindsay, N.G., Murphy, F.C., Walsh, J.J., Waterson, J., 1993. Outcrop studies of shale smears on fault surfaces. Special Publications International Association of Sedimentologist 15, 113–123.

Lunne, T., Long, M., Uzielli, M., 2007. Characterisation and engineering properties of troll clay. In: Tan, Phoon, Hight, Leroueil (Eds.), Characterisation and Engineering Properties of Natural Soils.

Lupini, J.F., Skinner, A.E., Vaughan, P.R., 1981. The drained residual strength of cohesive soils. Geotechnique 31, 181–213.

Mandl, G., 2000. Faulting in Brittle Rocks. Springer Verlag, Berlin, 434 p.

Mandl, G., de Jong, L.N.J., Maltha, A., 1977. Shear zones in granular material. An experimental study of their structure and mechanical genesis. Rock Mechanics 9, 95–144.

Manzocchi, T., Walsh, J.J., Nell, P., Yielding, G., 1999. Fault transmissibility multipliers for flow simulation models. Petroleum Geoscience 5, 53–63.

Naruk S.J., 2008. Empirical calibrations of proven sealing faults. Joint Meeting of the Geological Society of America, Soil Science Society of America, American Society of Agronomy, Crop Science Society of America, Gulf Coast Association of Geological Societies with the Gulf Coast Section of SEPM.

Nowacki, E.H.F., 1967. Anvendelse av ringskjærapparatet for studier av omrørte leireresegenskaper ved store deformasjoner. Det store eksamensarbeidet i Geoteknikk og fundamenteringslære. NTH, Trondheim.

Olson, R.E., 1974. Shearing strength of kaolinite, illite and montmorillonite. Journal of the Geotechnical Division, ASCE 100 (GT11), 1215–1299.

Rawling, G.C., Goodwin, L.B., 2006. Structural record of the mechanical evolution of mixed zones in faulted poorly lithified sediments, Rio Grande rift, New Mexico, USA. Journal of Structural Geology 28, 1623–1639.

Rutqvist, J., Birkholzer, J., Cappa, F., Tsang, C.-F., 2007. Estimating maximum sustainable injection pressure during geological sequestration of CO_2 using coupled fluid flow and geomechanical fault-slip analysis. Energy Conversion and Management 48, 1798–1807.

Rutter, E.H., Maddock, R.H., White, S.H., 1986. Comparative microstructures of natural and experimentally produce clay-bearing fault gouges. Pure and Applied Geophysics 124, 3–30.

Rykkelid, E., Skurtveit, E., 2008. Experimental work on unconsolidated sand: the effect of burial depth at time of deformation. In: Proceedings of the 42nd US Rock Mechanics Symposium and 2nd US-Canada Rock Mechanics Symposium, Paper No 08-236, San Francisco, June 29–July 2.

Sandbækken, G., Berre, T., Lacasse, S., 1986. In: Yong, R.N., Townsend, F.C. (Eds.), Oedometer Testing at the Norwegian Geotechnical Institute. Consolidation of Soils: Testing and Evaluation, ASTM STP 892. American Society for Testing and Materials, Philadelphia, pp. 329–353.

Sassa, K., Gonghui, W., Fukuoka, H., 2003. Performing undrained shear test on saturated sands in a new intelligent type ring shear apparatus. Geotechnical Testing Journal 26, 1–9.

Sibson, R.H., 2000. Fluid involvement in normal faulting. Journal of Geodynamics 29, 469–499.

Sperrevik, S., Færseth, R., Gabrielsen, R., 2000. Experiments on clay smear formation along faults. Petroleum Geoscience 6, 113–123.

Sperrevik, S., Gillespie, P.A., Fisher, Q.J., Halvorsen, T., Knipe, R.J., 2002. Empirical estimation of fault rock properties. In: Koestler, A.G., Hunsdale, R. (Eds.), Hydrocarbon Seal Quantification. Elsevier, Amsterdam, pp. 109–125.

Takahashi, M., 2003. Permeability change during experimental fault smearing. Journal of Geophysical Research 108, 2235.

Takizawa, S., Kamai, T., Matsukura, Y., 2005. Fluid pathways in the shearing zones of kaolin subjected to direct shear tests. Engineering Geology 78, 135–142.

Tika, T.E., Vaughan, P.R., Lemos, L.J., 1996. Fast shearing of pre-existing shear zones in soil. Geotechnique 46, 197–233.

Torabi, A., Braathen, A., Cuisiat, F., Fossen, H., 2007. Shear zones in porous sand: insights from ring-shear experiments and naturally deformed sandstones. Tectonophysics 437, 37–50.

van der Zee, W., Urai, J.L., 2005. Processes of normal fault evolution in a siliciclastic sequence: a case study from miri, sarawak, Malaysia. Journal of Structural Geology 27, 2281–2300.

Weber, K.J., Mandl, G., Pilaar, W.F., Lehner, F., Precious, R.G., 1978. The role of faults in hydrocarbon migration and trapping in Nigerian growth fault structures. In: 10th Annual Offshore Technology Conference Proceedings, vol. 4, pp. 2643–2653.

Wibberley, C.A.J., Yielding, G., Di Toro, G., 2008. Recent Advances in the Understanding of Fault Zone Internal Structure: A Review. In: Geological Society, London, Special Publications, vol. 299 5–33.

Wibberley, C.A.J., Shimamoto, T., 2003. Internal structure and permeability of major strike-slip fault zones: the median tectonic line in mie prefecture, southwest Japan. Journal of Structural Geology 25, 59–78.

Yielding, G., Freeman, B., Needham, T., 1997. Quantitative fault seal prediction. American Association of Petroleum Geologists Bulletin 81, 897–917.